

Experience of Using Synchrotron Radiation for Studying Detonation Processes

V. M. Titov,^{1,4} E. R. Pruel,^{1,4} K. A. Ten,^{1,4}
L. A. Luk'yanchikov,^{1,4} L. A. Merzhievskii,^{1,4}
B. P. Tolochko,³ V. V. Zhulanov,² and L. I. Shekhtman²

UDC 534.222.2

Translated from *Fizika Goreniya i Vzryva*, Vol. 47, No. 6, pp. 3–15, November–December, 2011.
Original article submitted March 22, 2011.

Results of studying detonation processes in condensed high explosives, which are obtained by methods based on using synchrotron radiation, are summarized. Beam parameters are given, and elements of the station and measurement system are described. Data on the density distribution in the detonation front for several high explosives are presented, and values of parameters in the Neumann spike and at the Jouguet point are determined. A method used to reconstruct a complete set of gas-dynamic characteristics (density fields, particle velocity vector, and pressure) from the experimentally measured dynamics of the x-ray shadow of the examined flow is described. Results of using this method for studying detonation of a charge of plastic-bonded TATB are presented. A method of measuring small-angle x-ray scattering in the course of detonation conversion is described. Based on results obtained by this method for a number of high explosives with an excess content of carbon, kinetics of condensation of free carbon and dynamics of the mean size of nanoparticles being formed thereby are analyzed.

Key words: synchrotron radiation, detonation, diagnostics, high explosives.

DOI:

INTRODUCTION

Aleshaev et al. [1, 2] proposed a method for studying detonation and shock-wave processes with the use of synchrotron radiation (SR) induced by operation of strong-current cyclic accelerators in the regime of pulsed generation of such radiation. The formation of a bunch of electrons on the orbit leads to generation of x-ray quantum pulses following each other with a stable time interval. A small duration of the pulse (≈ 1 nsec) en-

ures high accuracy of measuring the parameters of fast processes. During that time that passed after the papers [1, 2] were published, specialists of the Novosibirsk Scientific Center used the accelerators and other facilities of the Budker Institute of Nuclear Physics of the Siberian Branch of the Russian Academy of Sciences (BINP SB RAS) to perform a series of experiments in this field. Specialists from various institutes of Sarov, Snezhinsk, Moscow, and Chernogolovka participated in some experiments. The basic attention in this paper is paid to using synchrotron radiation for studying the processes of detonation of condensed high explosives (HEs), including problems of density measurements in the detonation wave and in the expanding explosion products, kinetics of formation of the condensed phase of carbon during detonation, and estimation of the size of nanoparticles (including nanodiamonds) being formed.

¹Lavrentyev Institute of Hydrodynamics, Siberian Branch, Russian Academy of Sciences, Novosibirsk 630090; merzh@hydro.nsc.ru, pru@hydro.nsc.ru.

²Budker Institute of Nuclear Physics, Siberian Branch, Russian Academy of Sciences, Novosibirsk 630090.

³Institute of Solid State Chemistry and Mechanochemistry, Siberian Branch, Russian Academy of Sciences, Novosibirsk 630128.

⁴Novosibirsk State University, Novosibirsk 630090.

GENERAL CHARACTERISTICS OF THE EQUIPMENT

In all experiments described in this paper, the SR source is the storage ring of the VEPP-3 facility based at BINP SB RAS. Electrons collected into one bunch with the energy of 2 GeV pass through a deflecting magnet (wiggler) with the magnetic field induction of 2 T and form an SR pulse with the photon energy of 10–30 keV. The resultant soft x-ray radiation in this range allows effective conduction of x-ray experiments with objects having the density of 0.5–3 g/cm². The x-ray component of SR offers some advantages in the dynamic experiment over the traditional sources of x-ray radiation: high intensity of the photon flux 10⁶ photons/mm² during one exposure, low angular convergence, and high stability and periodicity of radiation flashes exposure time ≈ 1 nsec and repetition period from 125 nsec and higher).

The most important element of the measurement system is the DIMEX linear detector of x-ray radiation [3], which was developed and fabricated at BINP SB RAS. The detector allows the x-ray radiation flux density distribution to be recorded during a time shorter than the interval between the pulses and has 256 (in the latest version, 512) channels 0.1 mm wide. The electronic circuit of the detector allows 32 frames to be recorded. The DIMEX detector was used in all experiments described here. Its spatial resolution is 0.1 mm at the 50% efficiency of detection for quanta with the energy of ≈ 30 keV. The detector aperture is 25.6 mm (in the latest version, 51.2 mm) in the direction of the measured coordinate and 2 mm in the transverse direction. The developed version is an ionization chamber with a gas electron amplifier separating the region of conversion of x-ray quanta from the gap where the charge is directed onto a scanning microband structure made with a step of 0.1 mm. The coordinate distribution of intensity is determined from the magnitude of the charge passing through each element of the scanning structure during the exposure time. If the ionization chamber is filled by a Xe—CO₂ mixture (80–dv20%) up to a pressure of 7 atm, the device ensures a resolution of 0.2 mm and detection efficiency of 50%. To reduce the overall large radiation load, a mechanical “fast shutter” (rotating copper disk with a notch) is placed ahead of the detector to ensure the time of detector exposure in the experiment for 40 μ sec only.

DENSITY MEASUREMENTS IN THE DETONATION WAVE FRONT

Numerous experimental methods based on various physical principles have been developed for studying detonation regimes and the structure of the chemical reaction zone. A brief analysis of these methods can be found in [4]. Obtaining experimental information on the detonation wave structure remains urgent because of the continuing discussion about the area of applicability of the Zel’dovich–Neumann–Döring model. Leaving aside the details of this discussion, we only mention some of numerous papers dealing with experimental investigations of the front structure: see, e.g., [5–8]. The use of SR allows implementation of a nonintrusive internal method of studying the parameters of the detonating HE charge in the region adjacent to the detonation front (including the front itself under certain conditions). The data for charges with a comparatively small diameter for pressed TNT, RDX, and 50/50 TNT/RDX alloy, which were obtained by this method, can be found in [4, 9]. The arrangement of experiments is shown in Fig. 1. The HE charge was aligned horizontally, and the plane of the SR beam passed through the axis of the examined charge. The SI beam width was 20 mm, and its thickness was 0.1 mm. The detonation front moving with a constant velocity stayed in the detection zone for several microseconds. The interval between the pulses was usually 500 nsec, which allowed us to obtain 3–5 pictures of the distribution of radiation passed along the axis. The radiation was detected by the DIMEX detector located parallel to the charge axis at a distance of ≈ 1 m.

Based on the degree of attenuation of radiation that passed through the sample, we determined the mass of the substance on the beam $m = \int \rho dl$ (l is the path covered by the beam in the charge and ρ is the current density at beam points). We performed independent calibrations of the detector, based on irradiating homogeneous plates made of the examined HE [4]. The SR pulse parameters are fairly stable, which allowed us to perform calibrations both before and after the experiment.

The following circumstances were taken into account in processing the recorded signal and its conversion to the dependence $\rho(z)$ (density distribution along the charge axis) [4, 9].

1. The detector used is designed in such a manner that the ingress of a γ -quantum of radiation into one detection channel gives rise to a charge not only in this channel, but also in the neighboring ones. As a result, the signal boundaries are “smeared” in space even if the irradiated object completely absorbs radiation. A

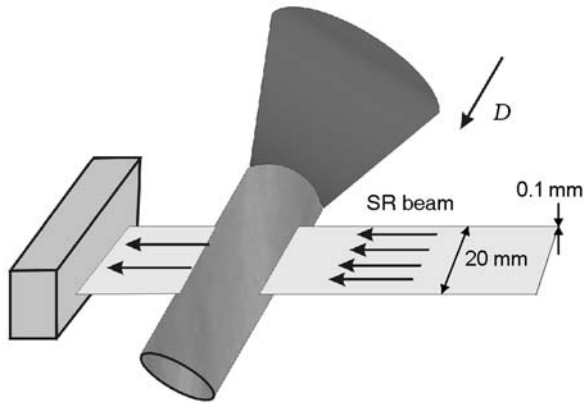


Fig. 1. Arrangement of experiments for studying the density in the detonation wave front.

special algorithm was developed to refine the detector data in the region of large density gradients. The algorithm is based on using an experimentally determined function of “instrumental widening.” Further testing of the correction algorithm capabilities showed that it can reconstruct the initial signal within 1%.

2. The real detonation wave front is not plane even in charges of sufficiently large diameters. In our case, we used small-diameter charges, where the front curvature increases and its projection covers approximately ten channels of the detector. The front shape was additionally studied in experiments with recording luminescence of detonation reaching the end face of the charge by means of high-speed filming. Therefore, when the detector data were converted to the dependence $\rho(z)$, the correction consisted of the following stages:

- the detonation wave front was assumed to consist of a set of layers with an identical curvature of constant density, which were shifted along the charge axis by the detector channel width;
- the shape of the layers was approximated by some part of a parabolic surface whose parameters were measured in experiments;
- the detector signal was calculated numerically with the use of calibration data and with due allowance for signal smearing in space;
- a discrete set of points of the distribution $\rho(z)$ was determined by varying the values under the condition of the best coincidence between the calculated value and the detector reading (the functional of root-mean-square deviations was minimized).

The correctness of the thus-obtained data was verified by comparisons with results of independent research [5–7]. Moreover, the measurements performed on charges of different diameters (TNT/RDX, Fig. 2) allow us to determine (similar to the method used in [6]) the

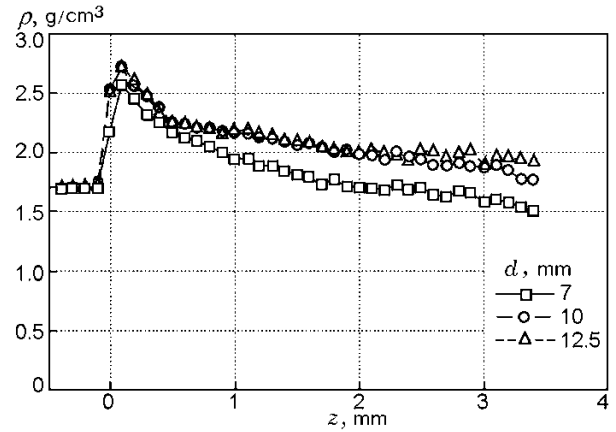


Fig. 2. Density distribution along the axis of cast TNT/RDX charges of different diameters.

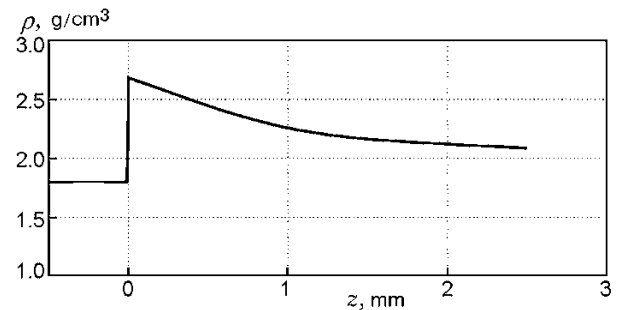


Fig. 3. Density distribution in TATB: the initial density is 1.85 g/cm^3 , and the detonation velocity is 7.5 km/sec .

parameters of the Chapman–Jouguet state as a state at the point of intersection of curve segments corresponding to self-similar unloading waves. A comparison confirmed that our results agree well with the data of other authors.

Figure 3 shows the results for TATB charges 20 mm in diameter. The corresponding results for an emulsion HE based on ammonium nitrate (EMX) are shown in Fig. 4. An additional analysis showed that the measurement error was $\approx 3.7\%$ [4, 9]. A complete list of parameters on the detonation front of examined HEs is given in Table 1.

TOMOGRAPHY OF GAS-DYNAMIC CHARACTERISTICS OF THE DETONATION FLOW

In experiments of this cycle, the detonating charge was probed in a plane perpendicular to the axis (Fig. 5). This arrangement allowed us to obtain data on the dy-

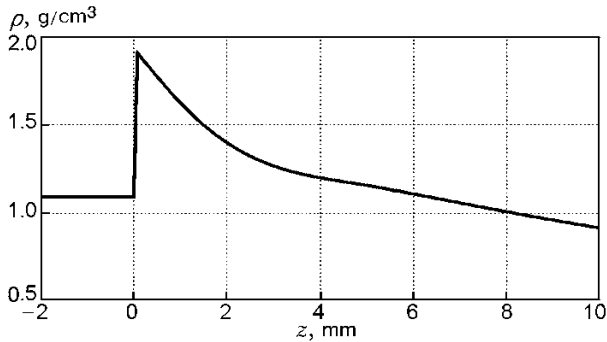


Fig. 4. Density distribution in the emulsion HE based on ammonium nitrate: the charge diameter is 20 mm, its density is 1.075 g/cm^3 , and the detonation velocity is 4 km/sec.

HE	ρ_N , g/cm^3	ρ_{CJ} , g/cm^3	τ , μsec	δ , mm
TNT	2.61	2.09	0.1 ± 0.014	0.7 ± 0.1
RDX	2.64	2.26	0.048 ± 0.012	0.4 ± 0.1
TATB	2.68	2.32	0.13 ± 0.013	1.1 ± 0.1
PST	2.65	2.22	0.15 ± 0.014	1.2 ± 0.1
EMX	1.81	1.37	0.75 ± 0.14	3.5 ± 0.4

Note. ρ_N is the density in the Neumann spike; ρ_{CJ} is the Chapman–Jouguet density; τ and δ are the front duration and width.

namics of the mass distribution on the beam in a fixed section of the examined detonation flow. An example of such a distribution is shown in Fig. 6. Actually, to obtain a tomographic image of an object, the latter should be photographed from different perspectives. For cylindrical charges, the flow of detonation products is axisymmetric. This fact allows us to reconstruct the density distribution along the radius in the examined charge section on the basis of information obtained by probing in one perspective only. Further, with the flow being assumed to be steady, we reconstruct the complete density distribution of detonation products (i.e., we construct the function $\rho(r, z)$, where r and z are the radial and axial coordinates). It is necessary to solve ill-posed inverse dynamic problem of tomography, and the classical methods based on Abel’s inversion cannot be used here [10, 11]. The reason is the non-smoothness of data obtained in experiments and the problem of their regularization. One possible solution of this problem is to develop special methods of density reconstruction, based on regularization of the sought density distribution with intense involvement of *a priori* information on the examined flow structure. In our case, we developed a special method of reconstructing gas-dynamic param-

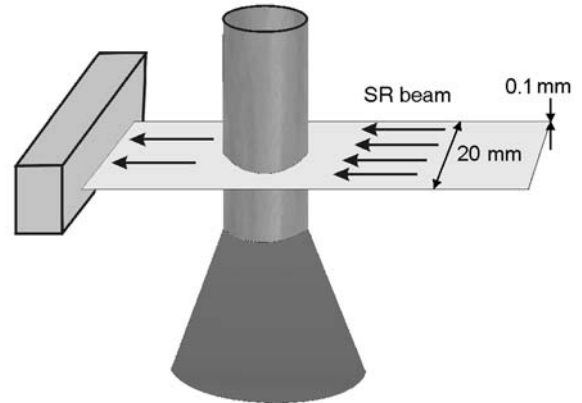


Fig. 5. Arrangement of the experiment on determining the density distribution in the detonation flow.

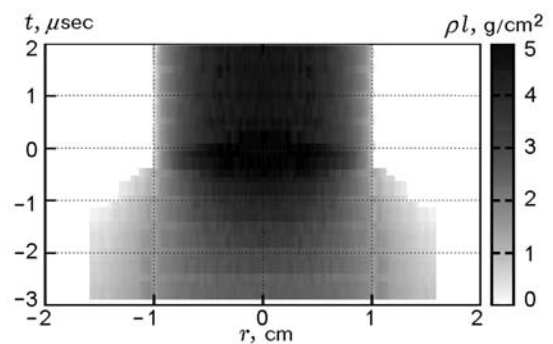


Fig. 6. Dynamics of the x-ray shadow in a fixed section during plastic-bonded TATB charge detonation.

eters of the detonation flow from the data of x-ray experiments. The method is rigorously tuned to a particular problem, but it ensures not only significant improvement of the density reconstruction accuracy [12–14], but also determination of the remaining gas-dynamic characteristics: distributions of particle velocity and pressure [15, 16]. The developed and implemented algorithm is described below.

ALGORITHM OF RECONSTRUCTION OF FLOW PARAMETERS AND RESULTS OBTAINED

The method of reconstructing the fields of gas-dynamic characteristics of the detonation flow is based on the numerical solution of the gas-dynamic problem formulated in accordance with a particular experiment. Let us consider a problem of a cylindrically symmetric gas flow. In this case, the equations of continuity and motion in the Eulerian coordinates have the form

$$\begin{aligned} \frac{\partial r \rho u}{\partial r} + \frac{\partial r \rho v}{\partial z} &= \frac{\partial r \rho}{\partial t}, \\ \frac{\partial r \rho u^2}{\partial r} + \frac{\partial r \rho u v}{\partial z} + r \frac{\partial p}{\partial r} &= \frac{\partial r \rho u}{\partial t}, \\ \frac{\partial r \rho v^2}{\partial z} + \frac{\partial r \rho u v}{\partial r} + r \frac{\partial p}{\partial z} &= \frac{\partial r \rho v}{\partial t}, \end{aligned}$$

where ρ is the density, p is the pressure, u and v are the axial and radial components of the velocity vector \mathbf{v} , r and z are the radial and axial coordinates in space, and t is the time. Passing to the Lagrangian coordinate system, we solve the problem of the gas flow having the equation of state

$$p(\rho) = p_0(\rho/\rho_{00})^{\gamma(\rho)}$$

(p_0 , ρ_{00} , and γ are parameters that have yet to be determined). With specified values of parameters, we calculate the flow field in which the density distribution can be compared with that obtained in experiments. The calculation was performed in a domain with a plane right boundary, which is consistent with the assumption on a plane detonation wave propagating over the charge with a constant velocity D . The problem formulation is illustrated in Fig. 7. The boundary condition on the input boundary was the inflow of the mass and momentum fluxes ($\rho_0 D$ and $\rho_0 D^2$, respectively); the boundary conditions on the other boundaries were determined by solving the Riemann problem on the interface between the detonation products and air. Using the Lagrangian coordinates, we were able to identify the detonation discontinuity naturally and to perform calculations only in the domain occupied by the detonation flow. Godunov's method was used for the numerical solution with varied values of the sought parameters.

The parameters to be determined were chosen by minimizing the functional of root-mean-square deviations of the calculated and experimental x-ray "shadows" of the examined flow in selected nodes of the computational domain. The dependence $\gamma(\rho)$ was approximated by a cubic spline. The resultant problem of multidimensional minimization was solved by the simplex method described and implemented in [17].

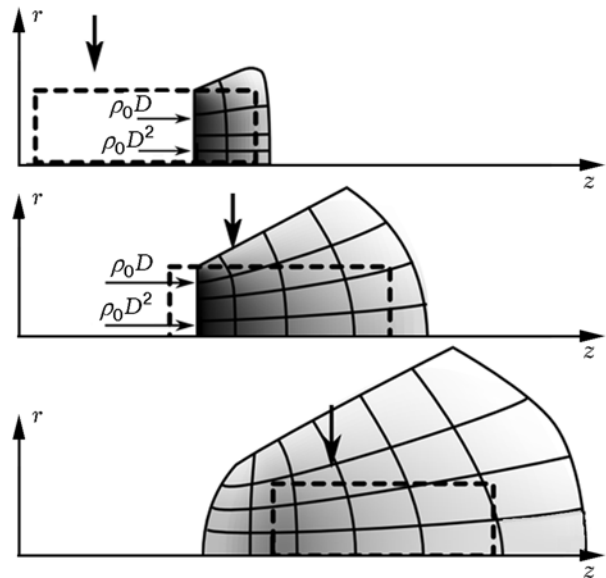


Fig. 7. Formulation of the gas-dynamic problem for calculating the detonation flow: the dashed curve shows the initial boundaries of the charge; the arrow indicates the location of the examined section.

The results obtained for a plastic-bonded TATB charge 20 mm in diameter are shown in Fig. 8. Figure 9 shows the calculated unloading adiabat (parameters along the streamline passing through the axis of symmetry). The calculated ratio of specific heats is close to the classical value $\gamma = 3$.

The system of equations used in the method for reconstructing flow characteristics does not involve the energy balance equation. This allows us to extend this method formally to the chemical conversion zone as well, though the assumptions made above become here somewhat incorrect. The real process in this zone is not isentropic, and the state cannot be considered as thermodynamically equilibrium. Nevertheless, the parameter distributions along the charge axis have regions of a drastic decrease in the values of the parameters, which can be approximately correlated with the chemical conversion zone. Continuing our considerations and interpreting the derivative $\partial p/\partial \rho$ as a squared velocity of sound c , we determine the position of the sonic surface from the equality $|\mathbf{v}| = c$, which is the Chapman–Jouguet condition in the coordinate system moving with the velocity of the detonation front. The thus-calculated sonic surface is shown in Fig. 10 (points on the dependences from Fig. 8).

The spatial error of reconstructing the flow characteristics is rather low: 1–2 detector channels, which is ≈ 0.2 mm. Based on the statistical data of three experiments with the interval between the frames of $0.5 \mu\text{sec}$,

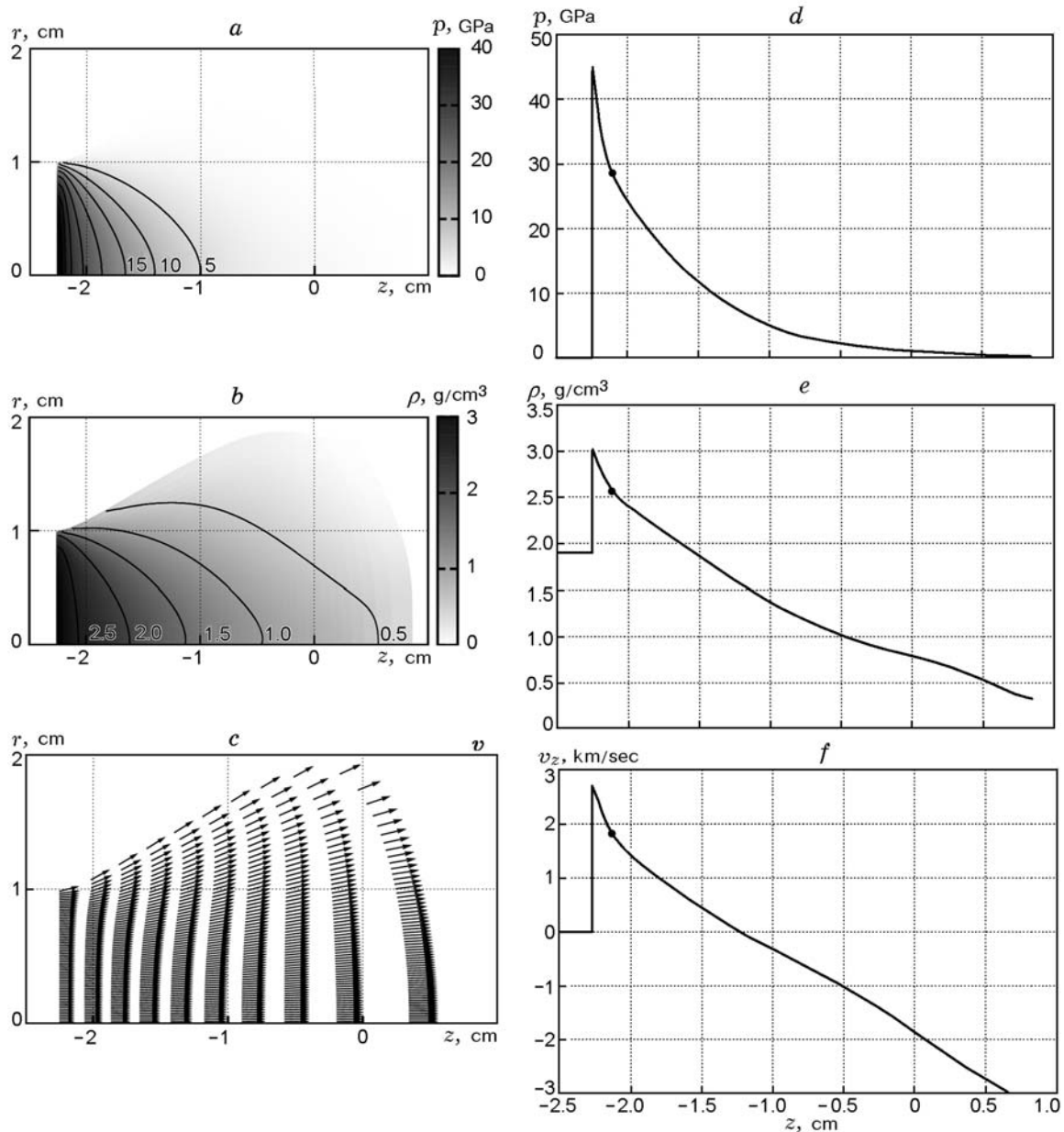


Fig. 8. Spatial distributions of parameters and their values on the axis during detonation of a cylindrical TATB charge (density 1.85 g/cm³) in 3 μ sec after initiation: (a) and (d) pressure; (b) and (e) density; (c) and (f) particle velocity in a fixed coordinate system; the point is the sonic boundary.

the overall time resolution is $\approx 0.2 \mu\text{sec}$. The accuracy of determining the values of the gas-dynamic characteristics is corrected by the conservation laws used and is estimated to be at least 90% at the time scale of 0.5 μsec . The values obtained in the energy release zone at the time scale of 0.2 μsec should be considered as estimates.

MEASUREMENT OF SMALL-ANGLE SCATTERING OF SYNCHROTRON RADIATION DURING HE DETONATION

Studying the processes of carbon condensation during HE detonation with a negative oxygen balance is extremely important for estimating the amount of energy released during exothermal coagulation of carbon clusters.

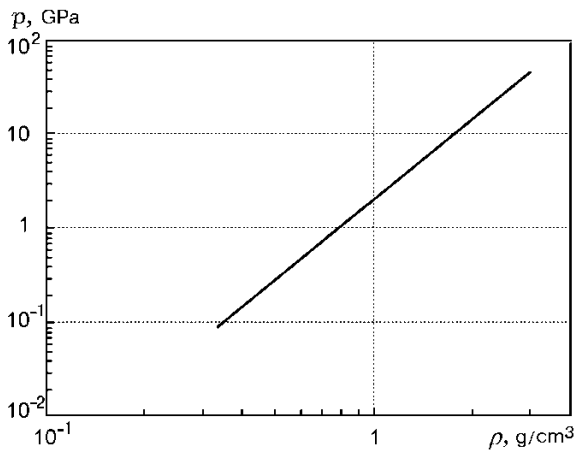


Fig. 9. Unloading adiabat of detonation products, constructed along the streamline passing through the charge axis.

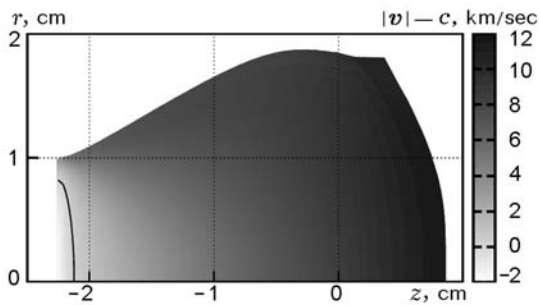


Fig. 10. Sonic boundary.

The published results [18, 19] showed that the assumption about carbon condensation behind the chemical reaction zone ensures a more accurate description of experimental data.

The problem was aggravated by the lack of methods that could detect the emergence of nanoparticles during the time of the detonation process in experiments. Now this can be done by diffraction techniques with the use of synchrotron radiation [20–22].

The method of measuring small-angle x-ray scattering (SAXS) is widely used in statistical analysis of the structure of disperse systems. Combining the SAXS method with SR generated by the VEPP-3 accelerator allows us to perform dynamic measurements of the angular distribution of SAXS. An analysis of the evolution of the SAXS distributions allows us to estimate the dynamics of the size of condensed nanoparticles during HE detonation.

SAXS theory. The use of the SAXS method al-

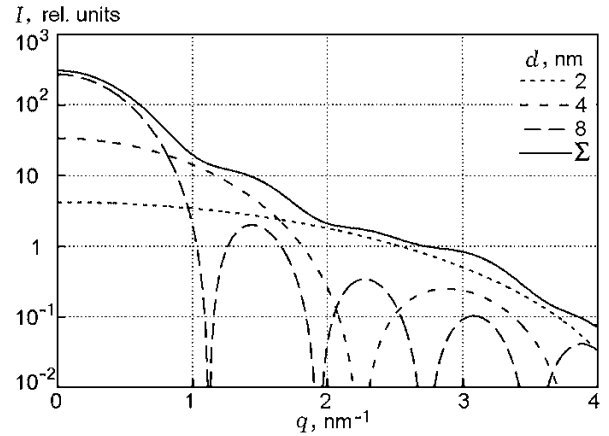


Fig. 11. Angular distributions of intensity for scattering on individual spherical particles of different diameters.

lows us to determine some averaged characteristics of the nanoparticle shape and structure. The particles can be in the solid, liquid, or gaseous state; the main point is the difference between their electron density and the medium density, i.e., the method is sensitive to “electron density fluctuations.”

In calculating the SAXS value for one particle consisting of many atoms, we sum up the interference of all electrons inside the particle. We assume that the particle has a spherical shape of radius R and the atoms (and electrons) inside the particle are uniformly distributed with a concentration n_e . The distance to the detector is $L \gg d$. Then, the amplitude of the scattered wave $E_s(q, R)$ in the vicinity of the detector is calculated analytically [23]:

$$E_s(q, R) \propto \frac{4\pi}{3} R^3 n_e \frac{3[\sin(qR) - (qR) \cos(qR)]}{(qR)^3}.$$

Here, $q = \frac{4\pi \sin \theta}{\lambda}$ is the absolute value of the scattering vector and 2θ is the scattering angle.

The total intensity of scattering on N randomly located particles is determined as

$$I(q, R) \propto N[E_s(q, R)]^2 = N \left(\frac{4\pi R^3 n_e}{3} \right)^2 P(q, R),$$

$$P(q, R) = \left\{ \frac{3[\sin(qR) - (qR) \cos(qR)]}{(qR)^3} \right\}^2.$$

The quantity $P(q, R)$ is called the shape factor. The angular distributions of intensity for scattering on individual spherical particles of different diameters are shown in Fig. 11.

If the scattering particle is located in a medium with an electron density n_0 rather than in vacuum, then

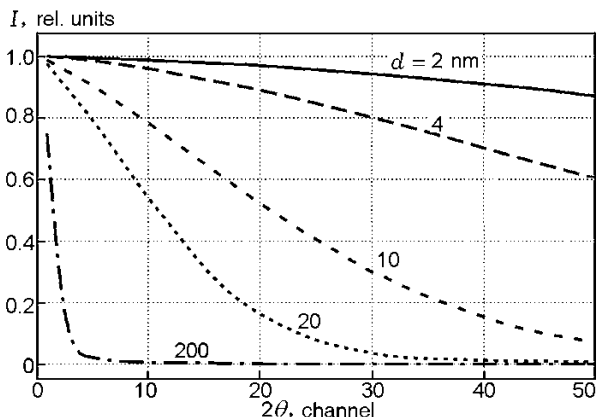


Fig. 12. Angular distribution of the SAXS signal from scattering particles of different diameters, calculated with allowance for the real spectrum.

the amplitude of the wave of scattered radiation is proportional to $(n - n_0)$, and the intensity is proportional to $(n - n_0)^2$ or, as researchers say, to the electron density “fluctuation.” In the case with a neutral (non-charged) sphere, the electron density is proportional to the density of the material of the scattering sphere, and the intensity of scattering on this sphere is determined as

$$I(q, R) \approx N \left(\frac{4\pi R^3}{3} \right)^2 (\rho - \rho_0)^2 P(q, R).$$

The squared difference of densities $(\rho - \rho_0)^2$ is often called the contrast.

The SR beam intensity provided by the VEPP-3 storage is insufficient for using a monochromatic spectrum in dynamic SAXS measurements because the intensity of scattered radiation is smaller than that of incident radiation by several orders of magnitude and because of a very short exposure time (≈ 1 nsec). For this reason, we used an SR beam with an initial polychromatic spectrum (energy 6–30 keV).

To estimate the SAXS distribution measured by the DIMEX detector, we performed model calculations of SAXS intensity for spherical particles 2, 4, 10, and 20 nm in diameter located in a TNT charge 20 mm in diameter. The calculations took into account the spectrum of VEPP-3 radiation and the spectral sensitivity of the DIMEX detector. Figure 12 shows the angular distributions of SAXS as functions of the particle diameter. The angle value is given in detector channels (one channel is equal to 0.1 mrad). It is seen in these figures that different particle diameters correspond to different slopes of the angular dependence of SAXS despite the polychromatic spectrum of SR, which means that the particle diameter in the range from 2 to 100 nm can be determined from the slope of the SAXS curves.

To estimate the size of the scattering particle in the formula for the shape factor, we expand the trigonometric functions into a Taylor series (the value of $x = qR$ in our conditions changes in the interval 0.012–0.63). After appropriate transformations, we obtain

$$P(q, R) \approx \left[1 - \frac{(qR)^2}{5} \right].$$

Then, the SAXS intensity (around zero) is

$$I(q, R) = I_0 \left[1 - \frac{(qR)^2}{5} \right],$$

where I_0 is the intensity in the zero angle. This function can be presented as the Ginnier relation for a spherical particle

$$I(q, R) = I_0 \exp \left[- \frac{(qR)^2}{5} \right].$$

From here, using the slope of the straight line in logarithmic coordinates, we can determine the scattering particle radius R .

In addition to the angular distribution of SAXS, it is of interest to consider the integral flux I_{int} of scattered radiation (it is found by means of summation over all angles and integration over the angle of revolution). It is insensitive to the particle size and shape and, with allowance for the contrast, yields the total mass of scattering inhomogeneities:

$$I_{int} = \int_0^\infty I(q) q^2 dq \propto \int_V (\rho - \rho_0)^2 dV.$$

The integral SAXS value strongly depends on the contrast, i.e., on the difference between the densities of the condensed particle and explosion products. For instance, the SAXS signal for nanodiamonds (density 3.5 g/cm³) is four times the signal for graphite (density 2.2 g/cm³) with the density of detonation products being 1.0 g/cm³. Thus, based on the integral SAXS value, we can estimate the phase composition of scattered nanoparticles.

Arrangement of experiments. For dynamic experiments with SAXS recording, we used the measurement system described in [20–22] and shown in Fig. 13. A band with a height of 0.4 to 1 mm and width of 3 to 16 mm was formed from the SR beam with the use of the lower (K_1) and upper (K_2) knives (Kratkey collimator) on the central part of the HE charge. Ahead of the detector, the straight beam was collimated again by another lower knife (K_3). The deflected SAXS beams were detected by the DIMEX detector. The angular range of SAXS measurements was $\approx 4 \cdot 10^{-4}$ – 10^{-2} rad (2–100 detector channels). This range of measurements allowed us to detect SAXS on particles with diameters d [23],

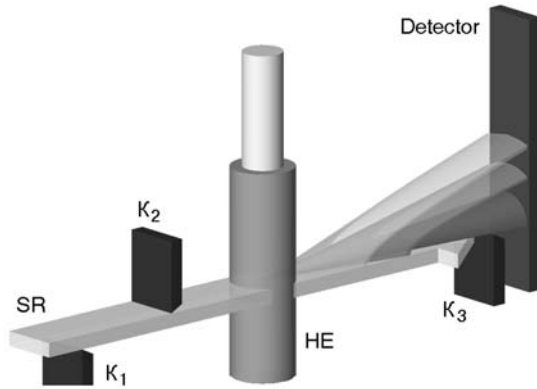


Fig. 13. Arrangement of experiments for SAXS measurements.

$d_{\min} \leq d \leq d_{\max}$, where $d_{\min} = \pi/q_{\max} = \lambda/(4\theta_{\max}) \approx 2.0$ nm and $d_{\max} = \pi/q_{\min} = \lambda/(4\theta_{\min}) \approx 75$ nm.

During one SR flash, the detector records all channels (makes one frame) with the SAXS distribution over the angle. As the detonation front moves along the charge with a constant velocity of 7.5 km/sec (for TATB), the detector records one more SAXS distribution (one more frame) after the SR pulse repetition period (250–500 nsec). Thus, a time sequence of SAXS distributions is formed. Actually, this is an x-ray diffraction movie with a time shift of $0.5 \mu\text{sec}$ and duration of each frame equal to 1 nsec.

We studied pressed charges of TNT, RDX, 50/50 TNT/RDX, BTF, and TATB-based mixtures. The charge diameter was 20 mm, and the charge length was varied from 30 to 32 mm. The original TNT and RDX were recrystallized in acetone, and then these HEs and their mixtures were pressed into pellets 10–12 mm high. The pellets were placed into an assembly (Fig. 14) and fixed by screws. Initiation was performed by a primer based on plastic-bonded PETN.

Results. The data in Fig. 15 illustrate the dynamics of the integral SAXS for several HEs. The value of I_{int} for TATB is obviously lower than for 50/50 TNT/RDX. This means that the scattering particles have a noticeably smaller size and lower density; most probably, they are of the graphite type. Nanodiamonds smaller than 2 nm can also be present, but they cannot be detected by this method. A significantly higher value of I_{int} for BTF is apparently caused by the emergence of coarser particles (nanodiamonds).

As was noted above, the experimentally measured SAXS signal is a product of the condensed phase concentration and the contrast factor. Taking into account that latter and knowing the density distribution, we can estimate the total fraction of condensed carbon without identifying the particle sizes (Fig. 16).



Fig. 14. General view of the test assembly.

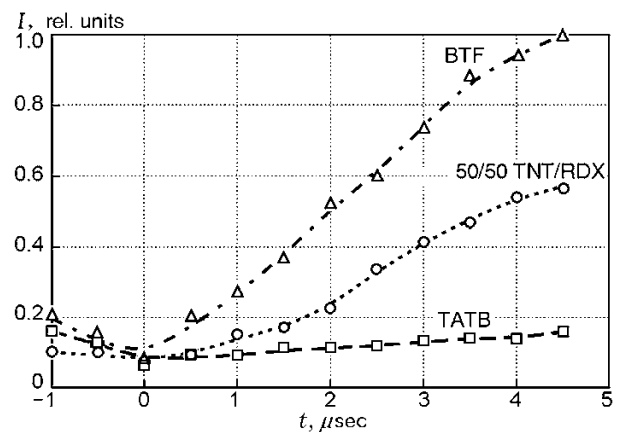


Fig. 15. Integral SAXS versus time.

The signal dynamics with allowance for varied density in expanding explosion products, which is shown in Fig. 16, allows us to estimate the time of carbon condensation as 1–2 μsec . The dynamics of the diffraction signal induced by detonation of a 50/50 TNT/RDX charge (density $\approx 1.7 \text{ g/cm}^3$) is illustrated in Fig. 17. The growth of the SAXS amplitude and the change in its angular distribution are seen. The scattering angle is given in detector channels (1 channel is equal to 0.1 mrad). The origin in this and further figures is at the instant of passage of the detonation front. Small initial SAXS is related to scattering on voids (pores) remaining

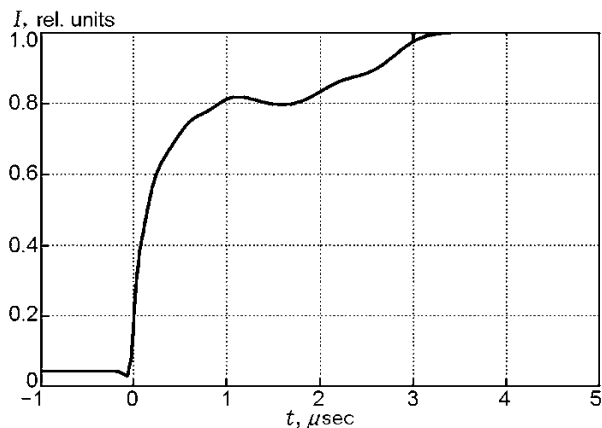


Fig. 16. SAXS signal with allowance for the effects of the contrast and attenuation of radiation for the 50/50 TNT/RDX charge.

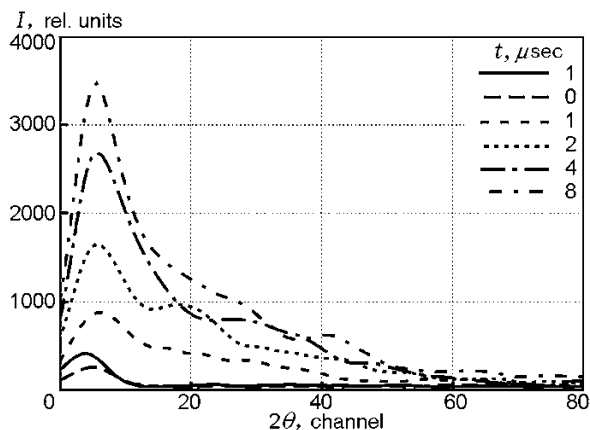


Fig. 17. Dynamics of the angular distribution of SAXS for 50/50 TNT/RDX.

after charge pressing. When the detonation front passes near them, the pores collapse and the minimum SAXS amplitude is observed. The emergence of SAXS and its enhancement are caused by the beginning of condensation of carbon nanoparticles and by an increase in their number and size (factor $n(R^3)^2$ in the formula given above). Moreover, the SAXS signal amplitude significantly increases with time owing to the increase in the “contrast” during expansion of detonation products (factor $(\rho - \rho_0)^2$ in the same formula). The change in the slope of the SAXS curve is related only to the increase in the scattering particle size (the shape factor $P(q, R)$ changes). The angular range of the noticeable SAXS signal for 50/50 TNT/RDX is approximately 100 detector channels or 10 mrad. Considerable “noise” on the curves is related to a small number of detected photons (10–30 scattered x-ray photons enter one detector channel).

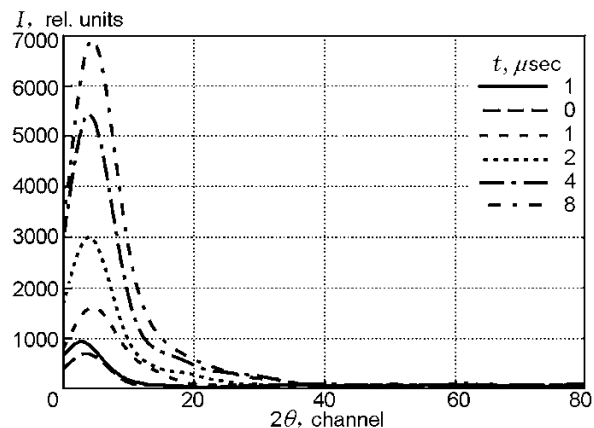


Fig. 18. Dynamics of the angular distribution of SAXS for BTF.

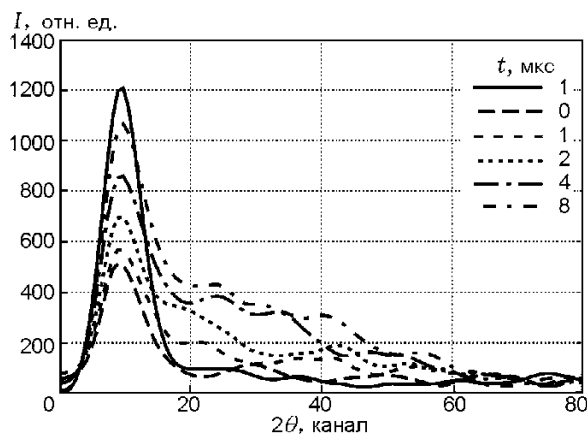


Fig. 19. Dynamics of the angular distribution of SAXS for TATB.

The behavior of the SAXS distribution for BTF (density 1.9 g/cm^3) (Fig. 18) is similar to the dynamics of 50/50 TNT/RDX, but the signal value (amplitude) is greater by an order of magnitude and the angular distribution is appreciably narrower (all radiation is within 5–7 detector channels). The signal-to-noise ratio is much better here.

The SAXS dynamics for TATB (density 1.85 g/cm^3) is illustrated in Fig. 19. The signal level is twice lower than for 50/50 TNT/RDX. A somewhat higher value of the initial SAXS can be caused by the presence of a large number of pores that are smaller than in charges of other HE types (the method does not capture “density fluctuations” greater than 0.1 μm).

Processing of the curves by the relations derived above allows us to estimate the dynamics of the condensed nanoparticle size (Fig. 20). It follows from the

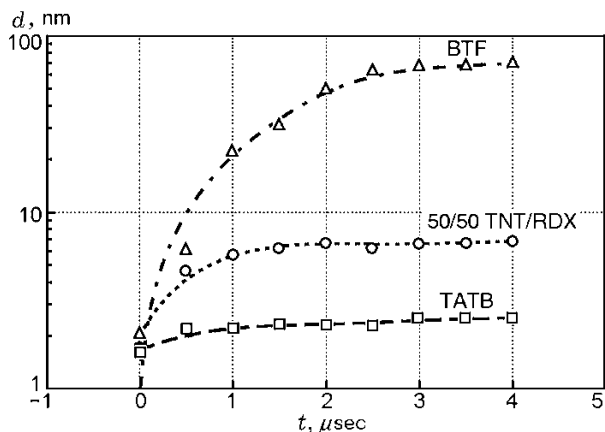


Fig. 20. Nanoparticle size versus time.

plots in Fig. 20 that nanoparticles with $d \approx 2$ nm are detected on the detonation front. Later on, the particle size increases and reaches $d \approx 2.5$ – 3.0 nm for TATB, ≈ 5 – 6 nm for 50/50 TNT/RDX, and 60–70 nm for BTF at the time $t = 2$ – 3 μsec . The data in Fig. 20 illustrate the range of capabilities of the method. The initial size of ≈ 2 nm is the lower limit, and the upper limit is ≈ 70 nm (final size for BTF). The nanoparticle sizes determined in dynamic experiments almost coincide with the data obtained in studying the collected explosion products [24, 25].

It should be noted that all HE charges in the experiments performed had an identical initial size; therefore, the “contrast” $((\rho - \rho_0)^2)$ during expansion of explosion products in experiments with different HEs varied more or less identically; as a result, the comparative difference in the amplitudes of scattered radiation intensity for these HEs is proportional to $N(R^3)^2$.

CONCLUSIONS

Methods developed on the basis of using synchrotron radiation offer new possibilities in studying detonation processes in condensed high explosives. In the case of steady detonation, we managed to measure the density distribution on the detonation wave front and in expanding products. A method of reconstruction of the remaining gas-dynamic characteristics of the flow of detonating charges (velocity and pressure) on the basis of the space and time distributions was proposed and tested. The results allowed us to reconstruct the unloading adiabat of detonation products. The use of the small-angle scattering effect provided new principal possibilities in studying nanoparticle condensation in detonation processes.

A permanently updated list of publications that describe activities with the use of synchrotron radiation for studying dynamic processes is available in the Internet [26].

The authors are grateful to specialists from the Budker Institute of Nuclear Physics of the Siberian Branch of the Russian Academy of Sciences G. N. Kulipanov, S. I. Mishnev, V. M. Aul’chenko, M. A. Sheromov, and others for their kind assistance in conducting experiments. The authors are also grateful to specialists of the Institute of Technical Physics B. G. Loboiko, A. K. Muzyra, Yu. A. Aminov, E. B. Smirnov, and O. V. Kostitsyn and to specialists from the Institute of Experimental Physics A. L. Andreevskikh, I. I. Karpenko, A. L. Mikhailov, and Yu. V. Sheikov for their assistance in preparing the examined materials and useful discussions.

This work was supported by the Integration Project Nos. 23 and 11 of the Siberian Branch of the Russian Academy of Sciences and by the Russian Foundation for Basic Research (Grant Nos. 08-03-00588, 11-03-00874, and 10-08-00859).

REFERENCES

1. A. N. Aleshaev, O. V. Evdokov, P. I. Zubkov, et al., “Application of synchrotron radiation for studying detonation and shock-wave processes,” Preprint No. 2000-92, Inst. Nuclear Phys., Sib. Branch, Russian Acad. of Sci., Novosibirsk (2000).
2. A. N. Aleshaev, P. I. Zubkov, G. N. Kulipanov, et al., “Application of synchrotron radiation for studying detonation and shock-wave processes,” *Combust., Expl., Shock Waves*, **37**, No. 5, 585–593 (2001).
3. V. M. Aul’chenko, O. V. Evdokov, I. L. Zhogin, et al., “Detector for studying explosive processes on a synchrotron radiation beam,” *Pribory Tekhn. Eksper.*, No. 2, 1–16 (2010).
4. K. A. Ten, O. V. Evdokov, I. L. Zhogin, et al., “Density distribution at the detonation front of cylindrical charges of small diameter,” *Combust., Expl., Shock Waves*, **43**, No. 2, 204–211 (2007).
5. L. V. Al’tshuler, G. S. Doronin, and V. S. Zhuchenko, “Detonation regimes and Jouguet parameters of condensed explosives,” *Combust., Expl., Shock Waves*, **25**, No. 2, 209–224 (1989).
6. V. K. Ashaev, G. S. Doronin, and A. D. Levin, “Detonation front structure in condensed high explosives,” *Combust., Expl., Shock Waves*, **24**, No. 1, 88–91 (1988).
7. B. G. Loboiko and S. N. Lyubyatinskii, “Reaction zones of detonating solid explosives,” *Combust., Expl., Shock Waves*, **36**, No. 6, 716–733 (2000).

8. A. V. Utkin, S. A. Lolesnikov, and V. E. Fortov, "Structure of a steady detonation wave in pressed RDX," *Dokl. Ross. Akad. Nauk*, **381**, No. 6, 760–762 (2001).
9. K. A. Ten, O. V. Evdokov, I. L. Zhogin, et al., "Measurement of the density distribution in detonation processes with the use of synchrotron radiation," Preprint No. 2005-30, Budker Inst. Nuclear Phys., Sib. Branch, Russian Acad. of Sci., Novosibirsk (2005).
10. V. V. Pickalov and N. G. Preobrazhenskii, *Reconstruction Tomography in Gas Dynamics and Plasma Physics* [in Russian], Nauka, Moscow (1987).
11. V. N. Kozlovskii, *Information in Pulsed X-Ray Imaging*, Inst. Technical Physics, Russian Federal Nuclear Center, Snezhinsk (2006).
12. E. R. Pruel, L. A. Merzhievskii, K. A. Ten, et al., "Density distribution of the expanding products of steady-state detonation of TNT," *Combust., Expl., Shock Waves*, **43**, No. 3, 355–364 (2007).
13. O. V. Evdokov, A. N. Kozyrev, V. V. Litvinenko, et al., "High-speed X-ray transmission tomography for detonation investigation," *Nucl. Instrum. and Methods in Phys. Res.*, **A575**, 116–120 (2007).
14. E. R. Pruel, K. A. Ten, V. M. Titov, et al. "X-ray transmission tomography for detonation investigation," in: *Proc. of 14th Intern. Detonation Symp. (2010)*, pp. 345–351.
15. K. A. Ten, E. R. Pruel, L. A. Merzhievsky, et al., "Tomography of the flow of detonation products using SR," *Nucl. Instrum. and Methods in Phys. Res.*, **A603**, 160–163 (2009).
16. K. A. Ten, V. M. Titov, E. R. Pruel, et al., "Study of explosive processes in detonating charges 20 mm in diameter with the use of synchrotron radiation," Preprint No. 2009-021, Budker Inst. Nuclear Phys., Sib. Branch, Russian Acad. of Sci., Novosibirsk (2009).
17. GNU Scientific Library. Documentation www.gnu.org/software/gsl.
18. C. M. Tarver, J. W. Kury, and R. D. Breithaupt, "Detonation waves in triaminotrinitrobenzene," *J. Appl. Phys.*, **82**, No. 8, 3771–3782 (1997).
19. K. F. Grebenkin, M. V. Taranik, and A. L. Zherebtsov, "Computer modeling of scale effects at heterogeneous HE detonation," in: *Proc. of 13th Symp. (Intern.) on Detonation*, Norfolk, USA (2006), pp. 496–505.
20. V. M. Titov, B. P. Tolochko, K. A. Ten, et al., "Where and when are nanodiamonds formed under explosion?" *Diamond and Related Materials*, **16**, No. 12, 2009–2013 (2007).
21. K. A. Ten, V. M. Aulchenko, L. A. Lukianchikov, et al., "Application of introduced nano-diamonds for the study of carbon condensation during detonation of condensed explosives," *Nucl. Instrum. and Methods in Phys. Res.*, **A603**, Nos. 1–2, 102–104 (2009).
22. K. A. Ten, V. M. Titov, E. R. Pruel, et al., "Measurements of SAXS signal during TATB detonation using synchrotron radiation," in: *Proc. of 14th Intern. Detonation Symp. (2010)*, pp. 387–391.
23. D. I. Svergun and L. A. Feigin, *Small-Angle X-Ray and Neutron Scattering* [in Russian], Nauka, Moscow (1986).
24. V. M. Titov, V. F. Anisichkin, and I. Yu. Mal'kov, "Synthesis of ultradispersed diamond in detonation waves," *Combust., Expl., Shock Waves*, **35**, No. 3, 372–379 (1989).
25. V. V. Danilenko, *Explosive Synthesis and Sintering of Diamonds* [in Russian], Energoatomizdat, Moscow (2003).
26. Bibliographic Reference Book on Using SR for Studying Dynamic Processes. — <http://ancient.hydro.nsc.ru/srexpl>.